Noname manuscript No.
(will be inserted by the editor)

Revisiting piezoelectric sensor calibration methods using elastodynamic stress waves

Rui Wu · Paul A. Selvadurai · Chaojian Chen · Omid Moradian

the date of receipt and acceptance should be inserted later

Abstract The application of absolutely calibrated piezoelectric (PZT) sensors is increasingly used to help interpret the information carried by radiated elastic waves in nondestructive evaluation and laboratory/*in situ* seismology. In this paper, we present the methodology based on the finite element method (FEM) to characterize PZT sensors. The FEM-based modelling tool is used to numerically compute the true Green's function between a ball impact source

Rui Wu

Department of Earth Sciences, ETH Zürich, Zürich, Switzerland

E-mail: rui.wu@erdw.ethz.ch

Paul A. Selvadurai

Swiss Seismological Service, ETH Zürich, Zürich, Switzerland

Chaojian Chen

Department of Earth Sciences, ETH Zürich, Zürich, Switzerland

Omid Moradian

Department of Earth Sciences, ETH Zürich, Zürich, Switzerland

and an array of PZT sensors to map active source to theoretical ground motion. Physical-based boundary conditions are adopted to better constrain the problem of elastic wave propagation, reflection and transmission in/on the elastic medium. The modelling methodology is first validated against the reference approach (generalized ray theory) and is then extended down to 1 kHz where elastic wave reflection and transmission along different types of boundaries are explored. We find the Green's functions calculated using physical-based boundaries have distinct differences between commonly employed idealized boundary conditions, especially around the anti-resonant and resonant frequencies. Unlike traditional methods that use singular ball drops, we find that each ball drop is only partially reliable over specific frequency bands. We demonstrate, by adding spectral constraints, that the individual instrumental responses are accurately cropped and linked together over 1 kHz to 1 MHz after which they overlap with little amplitude shift. This study finds that ball impacts with a broad range of diameters as well as the corresponding valid frequency bandwidth, are necessary to characterize broadband PZT sensors from 1 kHz to 1 MHz. This work bridges the gap between microcrack/damage mechanics and laboratory/*in situ* acoustic emissions (AEs) by unraveling sources in terms of the physics that generates AE signals.

Keywords Acoustic emission · piezoelectric sensor · absolute calibration · Green' function · Hertzian impact · spectral deconvolution

1 Introduction

As brittle materials are subjected to external stress in a laboratory setting, localized and rapid inelastic deformation events occur that are associated with the growth or appearance of small defects at the grain-scale (from microns to millimeters), which can generate acoustic emissions (AEs) [1–3]. These emissions can cause high-frequency vibrations, at frequencies ranging from tens of kHz to several MHz, and are recorded by piezoelectric (PZT) sensors at known locations. In the last decade, great effort has been made to improve the understanding of laboratory-generated AEs in a quantitative manner [4–9]. Meanwhile, to help manage the induced seismic risk in geoEnergy applications at the decameter scale [10], fracture-induced stress waves at frequencies ranging from hundreds of Hz to tens of kHz, referred as *in situ* AE, are also quantitatively studied by local down borehole networks of calibrated PZT sensors [11–15, among others]. These studies differ from previous AE studies, in that they characterized the absolute mechanical energy released by fracturing processes due to the radiated waves in the stressed solids instead of the traditional parametric analysis of the voltage measured by PZT sensors [16, 17].

Recent advances in both laboratory and *in situ* AE monitoring during fracturing experiments has greatly improved our understanding of microcrack mechanisms over broadband ranges of source dimension (microns to meters) and frequency (hundreds of Hz to several MHz). Prior to exploring such seismic characteristics, it is essential to absolutely characterize or calibrate the PZT sensors utilized in both *in situ* and laboratory applications so that the

information conveyed via the ground motions can be interpreted from the measured voltages [2, 18–20].

Green's functions, used to map active source to theoretical ground motion, are vitally important for PZT sensor characterization. Researcher [21] investigated Elastic stress wave propagation within a semi-infinite homogeneous and isotropic elastic plate, which was first solved [22] and known as "Lamb's problem". More specifically, Lamb's problem focuses on calculating the elastic disturbance caused by stress waves due to a point force in/on a half space. To find the solution of Lamb's problem (or "Green's function"), researchers numerically solved Lamb's problem starting from generalized ray theory [21, 23–25].

Two main concerns limit the application of the generalized ray theory to calculate Green's functions. First, the corner frequency of amplitude spectra of AE events could be as low as to 1 kHz [15]. To model this, we require the spectra of Green's functions down to 1 kHz to calibrate PZT sensors of the same frequency band. This requires large computational loads to obtain the huge number of possible ray paths of Green's functions. Second, sample finiteness makes the semi-infinite conditions associated with Lamb's problem unrealistic for laboratory investigations and, therefore, the ray paths of side reflections from a finite elastic plate are non-negligible.

The finite element method (FEM) based numerical method is an alternative approach to obtain the Green's function (NGF) with regard to elastodynamic wave propagation [26–28] where more realistic boundary conditions, similar

to that of an experimental configuration, can be modelled. Few researchers [29–31] performed FEM analysis with idealized or simplified boundary conditions to study the instrumental response of PZT sensors utilized in laboratory experiments. They obtained the ground motion down to 1 kHz at the location of receivers created by ball impacts of various sizes on the top surface of an elastic plate. Their approach by using conventional FEM codes and fine grids, however, requires huge computational costs to obtain relatively flat amplitude spectra of NGFs from 1 kHz to 1 MHz where the specified spectra resolution needs to be satisfied.

In this study, we used a state-of-art FEM-based solver to numerically calculating true Green's functions between 1 kHz to 1 MHz excited by a unit step force-time function. To improve the computational efficiency, we perform FEM modelings using a fine grid to compute Green's functions of high frequency, and using a coarse grid to obtain Green's funtions of low frequency. In course of modeling the low-frequency ground motions from 1 kHz to 100 kHz, physical-based boundary conditions are utilized in the FEM modeling to mimic the realistic experiments: elastic stress wave propagation, reflection and transmission in/on an elastic medium. The NGFs of a group of source-receiver pairs from 1 kHz to 1 MHz are obtained and then the corresponding displacement at the location of the receivers is derived.

We performed ball impact tests over a range of diameters and used PZT sensors to measure the vibration in terms of voltage signal. Our analysis characterizes the broadband instrumental responses through accurately cropping

(*primary*, *secondary* and *tertiary*) and linking (*primary* and *secondary*) a group of segmented instrument responses over valid frequency bands in line with the accuracy of FEM solutions and quality of experimental data. Moreover, we extend the instrumental response analysis from a single sensor to an array of PZT sensors at take-off angles taking account into their unique source-receiver characteristics.

2 Theoretical background and experimental setup

2.1 Instrumental response of PZT sensor

Fig. 1 shows six concepts from a source to the output voltage that are used in our analysis: (*1*) active source, (*2*) Green's function, (*3*) theoretical displacement, (*4*) instrumental response, (*5*) amplification and bandpass and (*6*) voltage signal. An active source is used to produce a rapid transient force $f_j(\boldsymbol{\xi}, \tau)$ in the j direction at point $\boldsymbol{\xi}$ and delayed time τ on the top surface of medium (Ω). Elastic waves propagate through the medium and the theoretical displacement is represented as $u_k(\mathbf{x}, t)$ in the k direction throughout the medium (Ω) at any location $\mathbf{x}$ and time t.

Since elastic wave propagation has linear time-invariant characteristics and due to the spatial reciprocity of the representation theorem [32], $u_k(\mathbf{x}, t)$ can be expressed as

$$u_k(\mathbf{x}, t) = g_{kj}(\mathbf{x}, t; \boldsymbol{\xi}, \tau) * f_j(\boldsymbol{\xi}, \tau), \tag{1}$$

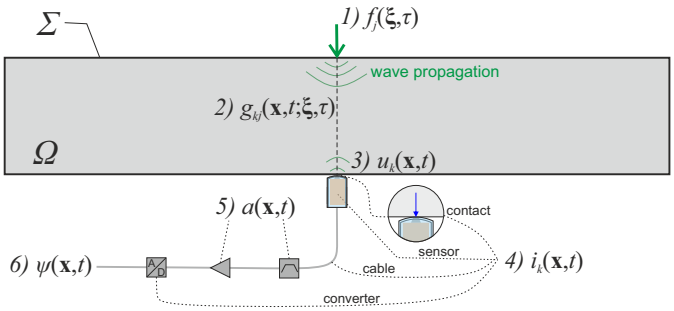

Fig. 1 Schematic drawing of concepts to illustrate the operation principle of PZT sensor that link the active source to generated voltage signals measured using a data acquisition system.

where * denotes the convolution operator, $g_{kj}(\mathbf{x}, t; \boldsymbol{\xi}, \tau)$ denotes the Green's function between the location of the source and receivers. Note that the assumption of point representation at the contact region of both the active source and PZT sensor is used, which is not exactly true due to finite area of the active source and the aperture area of the PZT sensors. This effect can be minimized by using a ball impact source and a conical-frustum PZT crystal with minimal contact area; this is discussed further in Section 2.2.

The time-varying displacement $u_k(\mathbf{x}, t)$ measured by the PZT sensors is then distorted into a voltage signal $\psi(\mathbf{x}, t)$, which is recorded by a connected data acquisition (DAQ) system. The instrumental response, $i_k(t)$, maps the true mechanical input u_k vibration in the k direction to the measured voltage $\psi(\mathbf{x}, t)$. The mapping is assumed to satisfy a linear time-invariant system such that

$$\psi(\mathbf{x}, t) = u_k(\mathbf{x}, t) * i_k(t) * a(t), \tag{2}$$

where $a(t)$ is the documented response of used amplifier including signal amplification, bandpass filter, etc. We aim to quantify the instrumental response of the PZT sensors, which integrates the effects of contact manner, intrinsic sensor characteristics, cables and analog/digital (A/D) converter. Note that if $a(t)$ is not available through experiments, the effect of $a(t)$ can be superposed into the final instrumental response.

We perform the deconvolution operation to Eq. (2) in the frequency domain to compute $I_k(\omega)$ as

$$I_k(\omega) = \frac{\Psi(\mathbf{x}, \omega)}{U_k(\mathbf{x}, \omega) A(\omega)}, \tag{3}$$

where ω denotes the ordinary frequency. $I_k(\omega)$, $\Psi(\mathbf{x}, \omega)$, $U_k(\omega)$ and $A(\omega)$ are variables in the frequency domain corresponding to $i_k(t)$, $\psi(\mathbf{x}, t)$, $u_k(\mathbf{x}, t)$ and $a(t)$, respectively.

To obtain an accurate instrumental response $I_k(\omega)$, we present the detailed analysis of acquiring voltage $\Psi(\mathbf{x}, \omega)$ in laboratory experiments (see Section 2.2) and numerically calculating Green's function $g_{kj}(\mathbf{x}, t; \boldsymbol{\xi}, \tau)$ (see Section 2.3). $A(\omega)$ used in this study is provided from [33]. The force-time function is determined from Hertzian impact theory [34] (see Appendix A).

2.2 Experimental setup: PZT sensor calibration station

In this section, we introduce the laboratory experiments performed on a sensor calibration station (see Fig. 2(a)). We characterize the performance of PZT

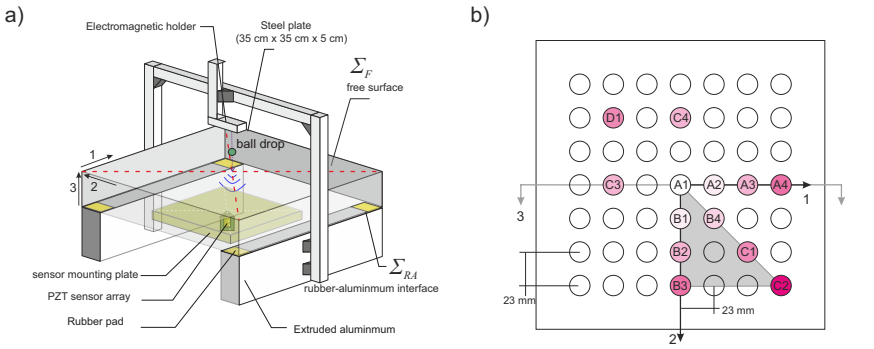

Fig. 2 (a) General schematic of calibration station in the *1-2-3* directions, which consists of electromagnetic holder, steel balls with different diameters, steel transfer plate, PZT sensor array, extruded aluminum framework, etc. (b) An array of PZT sensors, fixed by sensor mounting plate (yellow plate in (a)). Colors indicate their epicentral locations with respect to the source.

sensors to measured kinematic motion excited by elastic stress wave propagation through an elastic isotropic, homogeneous steel transfer plate due to the active source produced by a steel ball impact. A detailed comparison of characteristics, (dis)advantages and trade offs of laboratory active sources was explained in [35].

An extruded aluminum framework is used to support an overlaid square steel transfer plate (35 cm × 35 cm × 5 cm). Pads (4 yellow patches, 3 cm × 3 cm × 0.3 cm) made of nitrile butadiene rubber (NBR), with low mechanical impedance ($\sim 1/11$ of steel), are used to effectively block elastic wave refraction into the aluminum framework. An electromagnetic holder is built in the upper crossbeam of the aluminum framework. Once the power is turned off, the steel ball (green) is released and drops down freely until impact at the central location of the top surface of the steel transfer plate.

In Fig. 2(b), we show 13 PZT sensors with the same KRN Services (model KRNBB-PC) mounted at the bottom surface of the steel transfer plate. The array of PZT sensors has unique source-receiver characteristics that need to be accounted for [36, 37]. The sensor mounting plate has 7 × 7 locations with 23 mm spacing in both the *1* and *2* directions, respectively. Since stress waves caused by ball impact in the *3*-direction are symmetric about the *1-3* and *2-3* planes, we have focused most of our PZT sensor converge to one quadrant of the sensor mounting plate. In Fig. 2(b), similar colors for the PZT sensor locations (A1 to D1) represent the redundant epicentral locations with respect to the source. The darker to lighter colors represent the increasing epicentral locations. We use the take-off angle θ to characterize 7 possible seismic ray paths between the source and PZT sensors, $\theta = 0°$ (A1); 24.7° (A2, B1); 33.0° (B4); 42.6° (A3, B2, C3, C4); 52.4° (C1, D1); 54.0° (A3, B4); 62.9° (C2).

Note that the contact area between the circular tip of the KRNBB-PC sensors and the lower surface of the steel transfer plate has a radius of 0.75 mm, which is small relative to the dimension of the steel transfer plate. Also, the contact area between the ball and the upper surface of the steel transfer plate at the time of impact is negligible. Thus we assume that the point characteristics of the source and receiver in Section 2.1 is satisfied. No couplant (e.g. hot glue, Vaseline) is used through this study. These sensors are sensitive to ground motion in the *3*-direction over a wide frequency range (1

kHz to 1 MHz) and their spectral characteristics have been well documented [9, 25, 38, 39].

To acquire voltage $\psi(\mathbf{x}, t)$, a DAQ system (Elsys Instruments TraNET, 32 Channel TPCE-2016-4/8) is connected with the PZT sensors with a sampling frequency F_s of 20 MHz per channel. The Nyquist frequency is 10 MHz so that the F_s is adequate enough to perform sampling. Elsys AE amplifiers (AE-Amp) were used to provide the internal amplification [JFET, see 38] to sensors with 25 mA excitation and the gain was 0 dB.

To obtain instrumental responses, we perform Fast Fourier Transform (FFT) of the measured signals [40] over the frequency band from $1/T_w$ to $F_s/2$, where T_w is the time window and F_s is the sampling frequency. In this case, when the frequency approaches the lower bound $1/T_w$, low resolution of amplitude spectra can occur if not enough low-frequency cycles are analyzed. A proper time window T_w is critical to accommodate trade offs between spectra resolution and computational costs in modelling the excited elastic waves. We suggest that there should be at least $n = 8$ bins from the lowest frequency limit ($f_{min} =$ 1 kHz) to its adjacent frequency 2 kHz. Since the linearly spaced increment of frequency bins $\mathrm{d}f$ equals $1/T_w$, inequations can be given as

$$\frac{f_{\min} + n\frac{1}{T_w}}{f_{\min}} \leq 2, \tag{4}$$

$$T_w \geq \frac{n}{f_{\min}}, \tag{5}$$

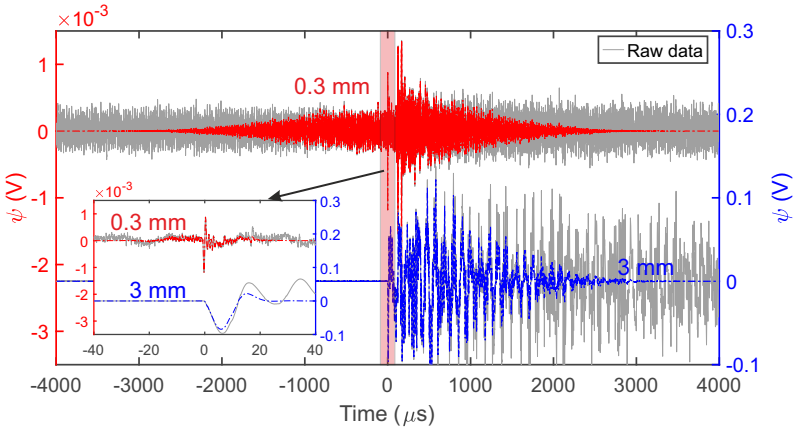

Fig. 3 Raw data (gray) and windowed data (colored) centered at the first P-wave arrival from typical acoustic events due to ball impact, with diameters of 0.3 (red) and 3 mm (blue), measured by the PZT sensor A1 located directly beneath the impact point. Window functions with two lengths 80 μs (see inset) and 8000 μs are used for high- and low-frequency analysis in B, respectively.

where a window length of $T_w = 8000$ μs is used to crop caused voltage $\psi(\mathbf{x}, t)$ and displacements $u_3(\mathbf{x}, t)$ with an identical length.

To avoid spectral leakage, a symmetric window function with the same length as $\psi(\mathbf{x}, t)$ and $u_3(\mathbf{x}, t)$ is essential. In Fig. 3, we show the raw data (gray line) of $\psi(\mathbf{x}, t)$ for typical acoustic events due to ball impacts with diameters of 0.3 and 3 mm. A 8000-μs Blackman–Harris window function $win(t)$ (centered about the first P-wave arrival) is used throughout this study to obtain windowed signals (red and blue lines). The windowed signals have the maximum in the middle, and taper away from the middle. By performing FFT to the windowed $\psi(\mathbf{x}, t)$ and $u_3(\mathbf{x}, t)$, and neglecting the phase information, we obtain

$$|U_3(\mathbf{x}, \omega)| = |\mathcal{F}\{g_{33}(\mathbf{x}, t; \boldsymbol{\xi}, \tau) * f_3(\boldsymbol{\xi}, \tau) \cdot win(t)\}|, \tag{6}$$

$$|\Psi(\mathbf{x},\omega)| = |\mathcal{F}\{\psi(\mathbf{x},t)\cdot win(t)\}|, \tag{7}$$

where $|U_3(\mathbf{x},\omega)|$ and $|\Psi(\mathbf{x},\omega)|$ are the amplitude spectra of windowed $\psi(\mathbf{x},t)$ and $u_3(\mathbf{x},t)$, respectively. $|\cdots|$ represents the absolute value operator. $g_{33}(\mathbf{x},t;\boldsymbol{\xi},\tau)$ is the *33*-component of Green's function that maps the ball drop impact force $f_3(\mathbf{x},t)$ in the *3*-direction to the measured displacement $u_3(\mathbf{x},t)$ in the *3*-direction. The details of Green's function are discussed further in Section 2.3.

Finally, Eq. (3) can be written as

$$I_3(\omega) = \frac{|\Psi(\mathbf{x},\omega)|}{|U_3(\mathbf{x},\omega)|A(\omega)} = \frac{|\mathcal{F}\{\psi(\mathbf{x},t)\cdot win(t)\}|}{|\mathcal{F}\{g_{33}(\mathbf{x},t;\boldsymbol{\xi},\tau) * f_3(\boldsymbol{\xi},\tau)\cdot win(t)\}|A(\omega)}, \tag{8}$$

where $\cdot$ denotes dot product, and $\mathcal{F}\{\}$ represents the FFT operation.

Material parameters of the steel ball, steel transfer plate and pad used in the calibration station are summarized in Table 1.

2.3 Green's function

We now aim to obtain Green's function, $g_{33}(\mathbf{x},t;\boldsymbol{\xi},\tau)$, which reflects the displacement component in the *3*-direction due to time-delayed Dirac delta (true impulse), $\delta(t-\tau)$ in the *3*-direction. However, it is not easy to implement $\delta(t-\tau)$ numerically. Instead, we use the Heaviside step function, $H(t-\tau)$,

Table 1 Material parameters of the steel ball, steel transfer plate and pad used in the calibration station.

Parameter	**Symbol**	**Value**		
		steel ball	steel transfer plate	pad
Type		GCr15	HABA CK45	NBR L8000
Young's modulus (GPa)	E	210	210	
Possion's ratio	ν	0.303	0.27	
Density (kg/m^3)	ρ	7800	7850	1490
P wave velocity (m/s)	c_p		5782	2690
S wave velocity (m/s)	c_s		3245	1340
Dimension (mm)		[0.3, 0.35, 0.4, 0.5, 0.6, 0.7, 0.8, 1.0, 1.5, 2.0, 2.5, 3.0]	350 × 350 × 50	30 × 30 × 3

which is the integral of $\delta(t-\tau)$ with respect to time. The corresponding $f_3(\boldsymbol{\xi}, \tau)$ can be expressed as

$$f_3(\boldsymbol{\xi}, \tau) = \delta(\mathbf{x} - \boldsymbol{\xi})H(t - \tau), \tag{9}$$

where $\delta(\boldsymbol{x} - \boldsymbol{\xi})$ denotes the spatial source distribution of the Dirac delta function. In this study, $\delta(\boldsymbol{x} - \boldsymbol{\xi})$ is described as a limit representation of the Dirac delta

$$\delta(\mathbf{x} - \boldsymbol{\xi}) = \lim_{S \to 0} \frac{1}{\sqrt{\pi S}} e^{-\frac{(\mathbf{x}-\boldsymbol{\xi})^2}{S}}, \tag{10}$$

where S is associated with the mesh size in the vicinity of the ideal loading point; its exact value is discussed in Section 3.2. The $u_3(\mathbf{x}, t)$ due to $f_3(\boldsymbol{\xi}, \tau)$ is given by

$$u_3(\mathbf{x}, t) = g_{33}(\mathbf{x}, t - \tau) * H(t - \tau). \tag{11}$$

Recalling the linear time-invariant characteristics of convolution in Section 2.1 and the properties of convolution differentiation [40], we can conduct time differentiation operation on Eq. (11) such that

$$v_3(\mathbf{x}, t) = g_{33}(\mathbf{x}, t). \tag{12}$$

Therefore, Green's function $g_{33}(\mathbf{x}, t)$ is derived as the particle motion velocity in the *3*-direction, $v_3(\mathbf{x}, t)$, caused by the force-time function $H(t - \tau)$ with a spatial distribution described by Eq. (10).

3 Numerical modelling of Green's function

In this section, we present the FEM-based methodology (i.e., governing equations, modelling parameters) to calculate NGFs. We validate the methodology against the reference approach over a high-frequency band (from 100 kHz to 1 MHz) and then extend it to low-frequency analysis down to 1 kHz.

3.1 Governing equations

We simulate the elastic wave propagation using the state-of-art discontinuous Galerkin (DG) FEM by COMSOL Multiphysics [41]. The steel transfer plate and pads are modelled explicitly and their material properties are provided in Table 1. The particle motion velocity, $\boldsymbol{v}$, and strain, $\boldsymbol{E}$, with the implementation for steel ($k = 1$) and rubber ($k = 2$) domains, obey the first-order elastodynamic equations

$$\rho^k \frac{\partial \boldsymbol{v}}{\partial t} - \nabla \cdot \boldsymbol{S} = \boldsymbol{f}, \tag{13a}$$

$$\frac{\partial \boldsymbol{E}}{\partial t} - \frac{1}{2}\left[\nabla \boldsymbol{v} + (\nabla \boldsymbol{v})^{\boldsymbol{T}}\right] = \boldsymbol{0}, \tag{13b}$$

$$\boldsymbol{S} = \boldsymbol{C}^k : \boldsymbol{E}, \tag{13c}$$

where ρ^k stands for the material density, $\boldsymbol{S}$ denotes the Cauchy stress tensor, and $\boldsymbol{f}$ is the applied loading described by Eq. (9). $\boldsymbol{C}^k$ represents the isotropic stiffness tensor characterized by Young's modulus, E, and Poisson's ratio, ν. To guarantee the uniqueness of $\boldsymbol{v}$ and $\boldsymbol{E}$, the zero-traction condition is enforced on the free surface Σ_{F} of the steel transfer plate, that is

$$\boldsymbol{n} \cdot \boldsymbol{S} = \boldsymbol{0}, \tag{14}$$

where $\boldsymbol{n}$ is unit normal vector. By incorporating numerical flux, DG FEM weakly imposes mechanical continuity of $\boldsymbol{v}$ and $\boldsymbol{E}$ across the interior boundary,

which is especially computationally efficient for studying 3D transient wave problems [27].

To model elastic stress wave transmission and reflection along the interface, Σ_{RA} (see Fig. 2(a)) between the pads and aluminum framework, we impose a velocity-dependent traction on Σ_{RA}. This traction is caused by the non-zero mechanical impedance of the aluminum framework ($k = 3$) and can be written as a combined effect of P- and S- waves [42]

$$\boldsymbol{n} \cdot \boldsymbol{S} = -\rho^k c_p^k \left(\boldsymbol{v} \cdot \boldsymbol{n}\right) \boldsymbol{n} - \rho^k c_s^k \left(\boldsymbol{v} \cdot \boldsymbol{t}\right) \boldsymbol{t}, \tag{15}$$

where ρ^k, c_p^k, c_s^k are the P- and S- wave velocity of aluminum, respectively, and $\boldsymbol{t}$ is the unit tangent vector. By adding this traction along Σ_{RA}, aluminum framework is not explicitly modelled.

3.2 Modelling parameters

In this section, we describe how the numerical calculations are performed to obtain NGFs, including the meshing schemes, time step and simulation procedures.

For meshing schemes, one of most critical issues is to choose an optimized mesh size; a relatively coarse grid works in a similar manner to a high-pass filter (HPF), leading to inaccurate NGF solutions whereas a very fine grid results in huge computational consumption (in terms of memory and CPU time). To produce a satisfactory solution, the maximum size h of the mesh

elements should be lower than the wavelength of interest λ. Since higher-order Lagrange interpolation functions, up to the forth order, are utilized, this ratio could be set as a larger value [41]. In this study, the ratio is assumed to be 1, that is $\frac{h}{\lambda} = 1$, where $\lambda = \frac{c_p}{\omega_0}$, λ, c_p denote the wavelength and velocity of P-wave, and ω_0 represents the upper limit of the bandwidth of interest. Even when using the efficient DG FEM, it is still time-consuming to calculate high-frequency NGFs. To reduce the computational cost, the adaptive grid scheme in FEM, can be adopted; however, this, is a non-trivial task. To remedy this, we introduce two separate simulations, which include a low-frequency model with a relatively coarse grid (*c-FEM*), and a high-frequency model with a relatively fine grid (*f-FEM*).

Due to the geometric symmetry of the calibration station, only $\frac{1}{8}$ of the steel transfer plate and pad was modelled. We set $\omega_0^c = 300$ kHz (>100 kHz) and $\omega_0^f = 1.2$ MHz (>1 MHz) to control h, where the superscripts c and f stand for *c-FEM* and *f-FEM*, respectively. The mesh around the center of loading area (red arrow) was locally refined to ensure a correctly applied $f_3(\boldsymbol{\xi}, \tau)$. We determine the S value from Eq. (10) as 1e-6 (units: $1/m^2$) by comparing the numerical integration of normal stress around the loading against $f_3(\boldsymbol{\xi}, \tau)$. The Delaunay tessellation method is adopted to create a tetrahedral mesh. Grid discretizations of models simulated in *c-FEM* and *f-FEM* are shown in Fig. 4(a) and (b), which have 762 and 104624 unstructured tetrahedral quartic elements, respectively. Details of material properties and the geometry information are given in Table 1.

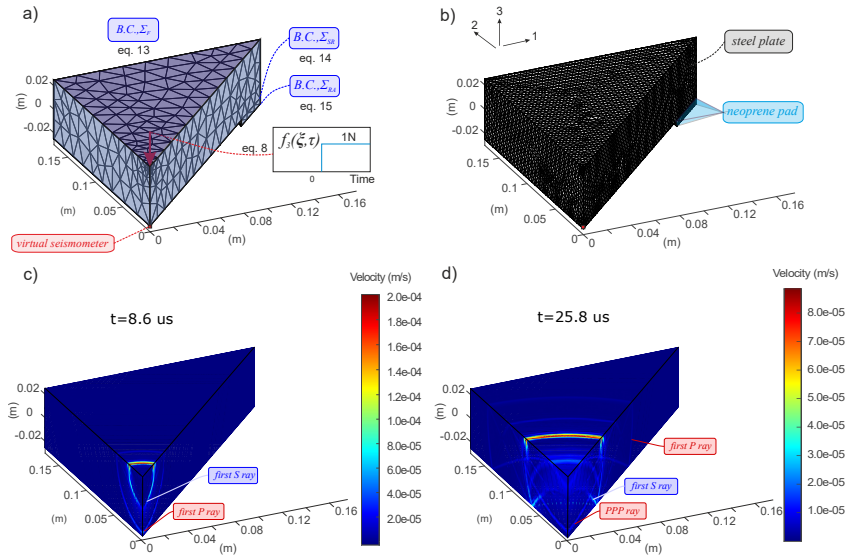

Fig. 4 1/8 symmetric modelling configuration visualized in the *1-2-3* directions to study laboratory elastic wave propagation caused by unit step force-time function. Boundary conditions are schematically shown to constrain the wave propagation problem. (a) *c-FEM* model with a coarse grid, (b) *f-FEM* model with a fine grid. The magnitude of the particle motion velocity field, acquired from the results of the *f-FEM* model, are visualized at time 8.6 μs (c) and 25.8 μs (d), respectively. Note that the time $t = 0$ is when the unit step force-time function is applied.

The Courant–Friedrichs–Lewy (CFL) condition is adopted to determine the stable time step, Δt, which is automatically optimized by COMSOL Multiphysics. During our simulations, the 4^{th} explicit Runge-Kutta (RK) method is adopted. Note that we use a pseudo-step loading scheme in the modellings. In this case, when we enforce a unit step force-time function to the loading point, there is a small 'rise time', τ_r, to reach the peak loading. By probing the real applied force history around the loading point (see arrow in Fig. 4), we found that τ_r is between 5 and 10 nanoseconds for *c-FEM* and *f-FEM*. Considering the fact that the force-time function of glass capillaries fracturing has a τ_r of approximately 200 nanoseconds while most of its spectral energy

does not fall below 2 MHz [9], this pseudo-step loading scheme has little effect on the spectrum over the bandwidth of interest.

For modelling procedures, we simulate *c-FEM* for 4000 μs and *f-FEM* for 40 μs (half length of suggested time window in Eq. (5)) such that the spectral resolution is satisfied down to 1 kHz and 100 kHz, respectively. The computational efficiencies of one FEM simulation are summarized. To perform the simulation of *c-FEM* for 4000 μs, 6 cores (41 hours for each core) and average memory 4.6 GB are required. Meanwhile, regarding simulating *f-FEM* for 40 μs, 16 cores (13.1 hours for each core) and average memory 13.3 GB are needed.

We obtain time-varying $v_3(\mathbf{x}, t)$ probed at the location of the virtual seismometer (red square in Fig. 4(a)) and derive the NGFs from both models by means of the transformation described by Eq. (12).

3.3 Model validation: high-frequency analysis of elastic waves

In above section, we propose using ω_0^c and ω_0^f to control the mesh size such that the frequency component of NGF can be expected to be kept below 100 kHz and 1 MHz. Our aim is to validate the capabilities of these models and find the corresponding valid frequency band beyond which the calculated NGFs deviate from reference results. Note that the reference ("true") results are computed by an approach based on the generalized ray theory (*GR*) [21, 24] that governs transient wave propagation in a semi-infinite purely elastic plate.

Fig. 4(c) and (d) show the magnitude of the particle motion velocity (units: m/s) to qualitatively illustrate the performance of the *f-FEM* model in simulating elastic wave propagation. We see that the elastic wave initiates from the loading point and geometrically spreads. Fig. 4(c) shows the first P-wave ray around the virtual seismometer and the first S-wave ray that follows at time 8.6 μs. The spatial distance between the wavefront of the first P- and S-wave is controlled by the wave propagation times and the speed difference between them.

In Fig. 4(d), we observe multiple reflections of different rays of the propagated elastic waves between the upper and lower surface of the steel plate at time 25.8 μs: first P-wave, first S-wave, PPP-wave, etc. The PPP-wave ray is shown around the virtual seismometer. These rays are important since they offer important information and frequency content in the velocity seismogram. We note that here we are only showing validation efforts for scenarios where the virtual seismometer is located directly below the source; however, this methodology can be extended to more source-receiver pairs (see Section 4.3), which will be a major benefit once the validation is complete.

We now validate the NGFs evaluated at the virtual seismometer over a short duration. The seismometer starts calculating $v_3(\mathbf{x}, t)$ from the instantaneous loading until the initial side reflection back. In our case, this duration is not allowed to exceed 60 μs so that NGF should, theoretically, be the same as that of the semi-infinite elastic plate since the wavefront has not reached

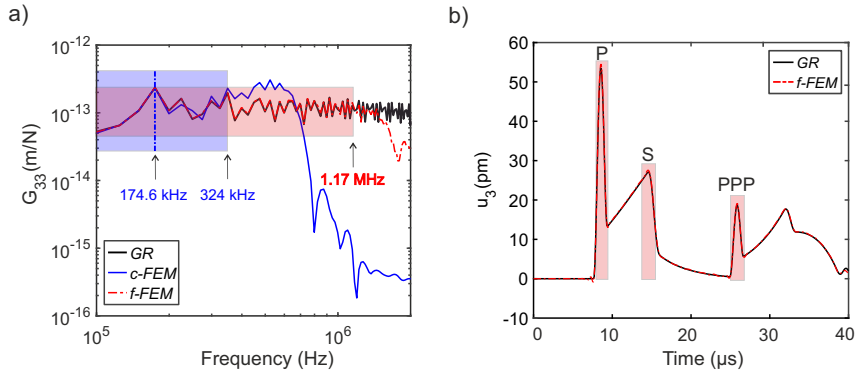

Fig. 5 (a) Green's functions from *GR* (black line), *c-FEM* (blue line) and *f-FEM* (red line) in frequency domain. The blue and pink patches mark the valid bandwidth where the modelling results match well with that of the generalized ray theory. (b) Theoretical ground motion from *GR* and *f-FEM* due to 0.5 mm ball impact. First P, S and reflected PPP phase of the elastic waves were captured and windowed inside the 3 pink bars, respectively.

the edges of the transfer plate. We simulated both *c-FEM* and *f-FEM* and the *GR* for 40 μs under the loading described by Eq. (9).

Fig. 5(a) shows the amplitude spectra of NGFs in the frequency domain. The amplitude spectrum calculated using the reference approach *GR* (black line) is almost flat below 2 MHz since the *GR* solution is semi-analytical. For NGFs from FEM modelling, the amplitude spectra match well with these of the *GR* when the frequency ranges from 100 to 324 kHz (for *c-FEM*, blue line) and from 100 to 1.17 MHz (for *f-FEM*, (red dash line)). However, the NGFs from both the *c-FEM* and *f-FEM* deviate rapidly from that of the *GR* around 324 kHz and 1.17 MHz, which corresponds approximately to the proposed ω_0^c and ω_0^f. The capabilities of both the *c-FEM* and *f-FEM* simulations are validated: we obtain accurate NGFs up to 100 kHz from the *c-FEM* and to 1 MHz from *f-FEM*. Note that to increase the accuracy of FEM solutions, we consider that the NGF from the *c-FEM* model is valid up to 174.6 kHz instead of 324 kHz.

After validating the capabilities of our built model with a simple geometry boundary, now we have a tool for studying elastic wave propagation that can accommodate realistic geometries with a validated level of accuracy. To have a better visualization in the accuracy of FEM solutions, Fig. 5(b) presents the theoretical displacement, $u_3(\mathbf{x}, t)$, in the *3*-direction from *GR* and *f-FEM* due to 0.5 mm ball impact (other parameters refer to Table 1) in the time domain. The $u_3(\mathbf{x}, t)$ from *f-FEM* is essentially equivalent to that of *GR*. First P, S and reflected PPP phase of the elastic waves were captured and windowed inside the 3 pink bars.

3.4 Model extension: low-frequency analysis of long-duration excitation down to 1 kHz

We extend the capability of *c-FEM* to perform low-frequency analysis by elongating the simulation duration. Due to the finite dimension of the calibration station, the simple Lamb problem, where only the elastic wave reflection between the bottom and top surface of the steel transfer plate is modelled, is no longer valid. To study the effects from boundaries on the elastic wave propagation problem, we conducted the following three modelling scenarios:

1. *float-NF*: modelling the elastic wave propagation through an unsupported/floating steel transfer plate. We adopt similar boundary conditions (free of stress over all surfaces of the tested specimen) to those used in [31] and construct a *float* model.

2. *float-HP*: in the *float* model, rigid body motion occurs because there are no constraints from the supported material (i.e., the pad beneath the steel plate) are modelled. To correct the NGFs imposed by improper boundary conditions, we process the raw $v_{33}(\mathbf{x}, t)$ using a minimum-order high-pass filter.
3. *true BC*: to better model the real elastic wave propagation, more physical boundary conditions, described by Eqs. (14) and (15) were already introduced in the *c-FEM* model to simulate the elastic wave reflection and refraction occurring at the interfaces of the steel transfer plate, pads and aluminum framework.

We extract $v_{33}(\mathbf{x}, t)$ with a duration of 8000 μs (centered at the first P-wave arrival) in the above scenarios and use the transformation (see Eq. (12)) to obtain the NGFs for the same source-receiver pair. By performing FFT and neglecting the phase information, we obtain the amplitude spectra of low-frequency NGFs, which are termed as *float-NF* (blue line in Fig. 6(a)), *float-HP* (black line in Fig. 6(a)) and *true BC* (red line in Fig. 6(a)) corresponding to the three scenarios given above, respectively.

In Fig. 6(a), *float-NF* tends to decrease 'linearly' from ∼1e-12 to ∼1e-14 m/N from 1 kHz and 100 kHz. The large amplitude of low-frequency components is caused by the rigid body motion of the steel transfer plate. By performing a high-pass filter operation on *float-NF*, the rigid body motion is significantly removed. We see that the *float-HP* has a relatively flat spectrum with few distinct spectral peaks representing the low-frequency resonances

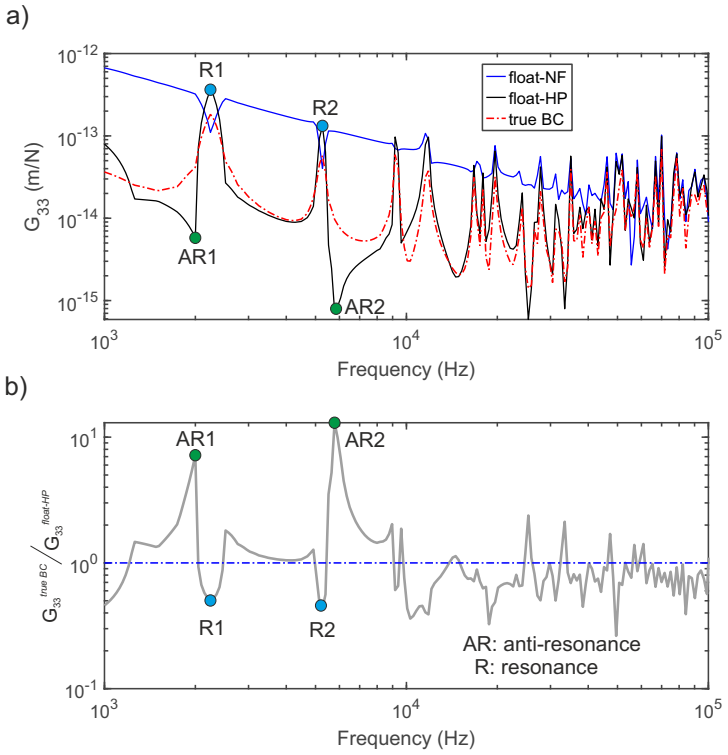

Fig. 6 (a) Comparison of NGFs calculated from three modelling scenarios: *float-NF* (blue line), *float-HP* (black line) and *true BC* (red line). (b) Ratio of NGFs from *true BC* to that of *float-HP*. Locations of resonant and anti-resonant frequencies are labelled as R and AR, respectively.

and anti-resonances of mechanical vibration. The resonant frequencies from *float-HP* and *true BC* match well over 1 to 100 kHz, demonstrating that a consideration of the true physical boundaries has little effect on the shift of the resonant frequency.

For a better comparison, we plot the ratio of *true BC* to *float-HP* from 1 to 100 kHz in Fig. 6(b). From 1 to 10 kHz, the ratio at the locations of resonant and anti-resonant frequencies deviates significantly from 1. These locations are labelled AR (anti-resonance) and R (resonance). We find that around the

resonant frequency (i.e., *R1* and *R2*), the *true BC* is nearly half the *float-HP*. Conversely, around the anti-resonant frequency, the *true BC* can be 7 to 13 times than of the *float-HP*. This ratio tends to be flat and close to 1 for frequencies between 10 to 100 kHz. This suggests that both scenarios have similar NGFs over 10 to 100 kHz.

We modelled how the physical constraints resulting from the experimental configuration affected the elastic wave propagation problem. We interpret the results from the physical-based boundary conditions. Kinematic energy of the elastic stress waves initially flows from the loading point, travels through the steel transfer plate and pads, and finally leaves the *c-FEM* model naturally where the spatiotemporal evolution of the energy field is dominated by properties of both media (steel plate, pads) and their interfaces. No extra high-pass filter operation is needed to remove the low-frequency component of the kinematic energy, which is fully trapped inside the steel transfer plate in the *float* model. Therefore, the constructed *c-FEM* model can be utilized to obtain the NGF in a more physical way, which becomes important when more complex geometries and boundary conditions are applied. To solve the multiphysics problem of elastic wave propagation, our constructed models can potentially be integrated with state-of-the-art multiphysics couplings (i.e. temperature and fluids) from the COMSOL Multiphysics software whose abilities have been validated against theoretical solutions and/or laboratory experiments in the geomechanics communities [43–46].

4 Broadband Characterization of PZT sensors

In the above sections, we described the FEM-based methodology used to obtain high-frequency NGFs from 100 kHz to 1 MHz as well as low-frequency counterparts from 1 to 100 kHz. By performing ball impact experiments, we presented the displacement $|U_3|^{s,l}_{\chi}$ and voltage spectra $|\psi|^{s,l}_{\chi}$ in short- (denoted by s, 100 kHz to 1 MHz) and long-duration (denoted by l, 1 kHz to 100 kHz) excitation in Appendix B. Label χ denotes an unique ball diameter, $\chi \in [1, N]$, where N is the number of ball sizes. In this section, we obtain a group of segmented instrumental responses $I^{s,l}_{3,\chi}$ with different forces and duration of ball impact in accordance with Eq. (8). We develop an algorithm of spectrum cropping and linking to integrate a group of $I^{s,l}_{3,\chi}$ into a truly broadband understanding of I_3 from 1 kHz to 1 MHz for single sensor as well as an array of PZT sensors with unique source-receiver characteristics.

4.1 Algorithm to integrate segmented instrumental responses

We are reminded of the fact that a specific member of the $I^{s,l}_{3,\chi}$ group is not valid over the whole frequency bandwidth. Instead, the accuracy of $I^{s,l}_{3,\chi}$ is regulated by the quality of the experimental data (i.e., corner frequency ω_c of voltage spectra $|\Psi|^{s,l}$, signal-to-noise ratio or SNR, variations among repeated tests) and the solution accuracy of the FEM modelling. If we perform a simple union operation of the $I^{s,l}_{3,\chi}$ group, the broadband I_3 will be distorted, with various level of uncertainty, by introducing all the components of $I^{s,l}_{3,\chi}$. To

obtain a more accurate I_3, we need to perform several 'cropping' operations to constrain the $I^{s,l}_{3,\chi}$ group.

The accuracy of FEM solutions is closely correlated with the mesh discretization. In high-frequency analysis, $I^{s}_{3,\chi}$ is picked from 100 kHz (the lower bound of the valid frequency band for the *f-FEM* model) to the corner frequency ω_c of voltage spectra $|\Psi|^s$. In low-frequency analysis, $I^{l}_{3,\chi}$ is cropped from 1 kHz to the minimum between 174.6 kHz (the upper bound of the valid frequency band of the *c-FEM* model) and ω_c of $|\Psi|^l$. This *primary cropping* operation can be denoted as $/\cdots/$ such that $/\left|I^{s,l}_{3,\chi}\right|/$ is obtained.

The quality of the experimental data is mainly controlled by the SNR (or ball size: large ball impacts generate higher SNR) and the repeatability of the test data. To alleviate the effect of background noise, a *secondary cropping* operation is proposed to better select the frequency band of $I^{s,l}_{3,\chi}$ based on the criterion of SNR > 1. We denote this as $\langle\cdots\rangle$ and obtain $\left\langle/\left|I^{s,l}_{3,\chi}\right|/\right\rangle$. In this case, the small ball impact has a limited contribution to the broadband I_3 due to its low SNR especially at the low-frequency range. We have illustrated the repeatably of ball impact tests in Appendix B, but there exists an amplitude offset of $I^{s,l}_{3,\chi}$ during repeated tests. We therefore remove the frequency band where the relative standard deviation of $|\Psi|^{s,l}$ is larger than specified threshold (2 % used in this study). We then average $I^{s,l}_{3,\chi}$ over the rest of the frequency band to get $\overline{\langle/\,|I_{3,\chi}|\,/\rangle}$; this *tertiary cropping* operation as $\overline{\cdots}$ is denoted.

Once the above 'cropping' operations are implemented, the $I^{s}_{3,\chi}$ group is well constrained. We now need to link all the cropped $I^{s}_{3,\chi}$ together from the

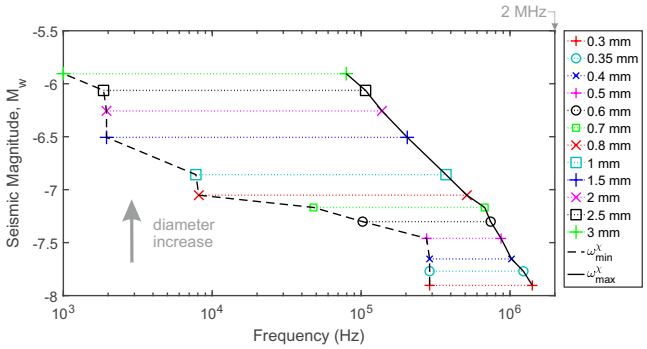

Fig. 7 Seismic magnitude M_w versus valid frequency band from a series of repeated ball drop tests (marker symbols) with diameters ranging from 0.3 to 3mm.

low- and high-frequency analyses over a broad range of ball diameters. The final broadband I_3 is written as

$$I_3 = \sum_{\chi=1}^{N} \overline{\langle / |\, I^l_{3,\chi} |\, / \rangle} \cup \overline{\langle / |\, I^s_{3,\chi} |\, / \rangle}, \tag{16}$$

where $\cup$ is the *primary link* operation between the low- and high-frequency cases, $\sum$ denotes the *secondary link* operation over different ball diameters. To help understanding the used algorithm, we present the general principle and flowchart of cropping and linking operations in Appendix C.

In Fig. 7, we present the caused seismic magnitude M_w versus valid frequency band of the grouped ball impacts. Note that M_w due to external ball impact is estimated from [47]. The region between ω_χ^{min} (black dashed line) and ω_χ^{max} (black solid line) suggests that these overlapped frequency bands of ball drops could fully cover the frequency scope of interest (from 1 kHz to 1 MHz). Here ω_χ^{min} and ω_χ^{max} represent the minimum and maximum valid frequencies of ball drops, respectively. We see that the results from ball impact

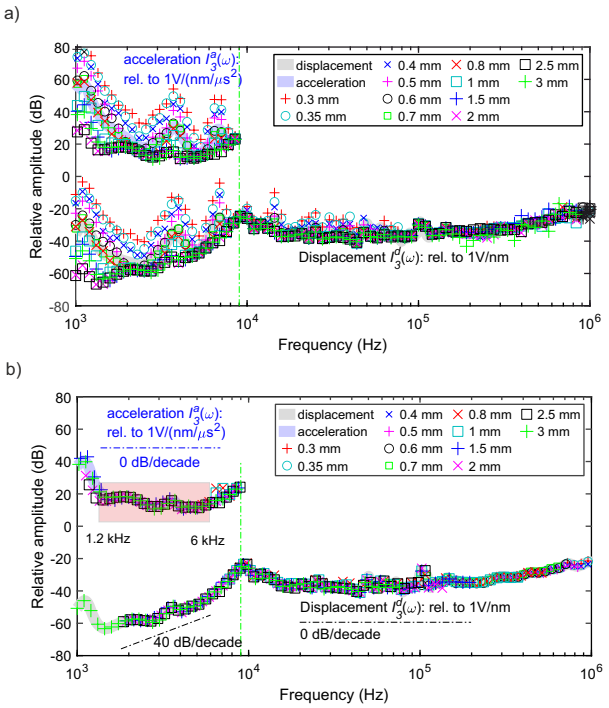

Fig. 8 (a) Original and (b) cropped displacement-based (gray thick line) and acceleration-based (blue thick line) instrumental response of a single PZT sensor from a series of repeated ball drop tests (marker symbols) with diameters ranging from 0.3 to 3 mm.

tests with diameters of 0.4, 1 and 3 mm almost cover broadband frequency range. This provides researchers with straightforward instructions about how to choose the right parameters for ball impact tests in accordance with their frequency range of interest when performing PZT sensor characterization.

4.2 Single PZT sensor: broadband I_3

In this section, we illustrate the differences in the calculated broadband instrumental response I_3 of a single PZT sensor with and without cropping algorithm (see Eq. (16)). In the lower part of Fig. 8(a), we show the original

I_3^d in a marker symbol series from 1 kHz to 1 MHz (units: dB, the superscript d denotes displacement). We use 1 V/nm as the reference sensitivity of the PZT sensors to measured displacement. We see that, without cropping some components from the final I_3, there are remarkable amplitude variations of I_3^d in the frequency bandwidth of 1 to 7 kHz and 14 to 170 kHz, respectively.

Following the proposed algorithm described in Eq. (16), we obtain the cropped broadband I_3^d. In the lower part of Fig. 8(b), we see that the 12 data series (for 0.3 to 3 mm ball diameters) overlap with negligible vertical shift. This suggests a promising stability of the developed algorithm, as well as the characterization methodology. The linked I_3^d (gray thick line) is almost flat from 10 kHz to 1 MHz with a slope of nearly 0 dB/decade and shows a strong dependence on the measured displacement. We suggest that the PZT sensors used in this study can be used as a displacement-sensitive transducer from 10 kHz to 1 MHz. In the left lower part of Fig. 8(b), from 1 to 10 kHz, the linked I_3^d has a slope of 40 dB/decade.

By performing the transformation of displacement into acceleration in the frequency domain, we rewrite the displacement-based I_3^d into the acceleration-based I_3^a as

$$I_3^a = \frac{I_3^d}{(2\pi\omega)^2}, \tag{17}$$

where the superscript a denotes acceleration. We add the original and cropped I_3^a into Fig. 8(a) and (b), respectively. In Fig. 8(a), we find remarkable amplitude variations for the data series of I_3^a from 1 to 7 kHz. In Fig. 8(b), we

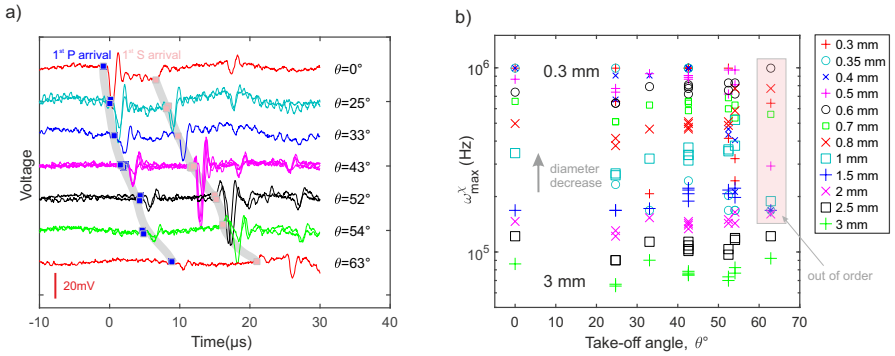

Fig. 9 (a) Raw voltage signals (colored) measured by a PZT sensor array at a group of take-off angles caused by a 0.5 mm diameter ball impact. (b) The maximum valid frequency versus take-off angle with ball diameters ranging from 0.3 to 3 mm.

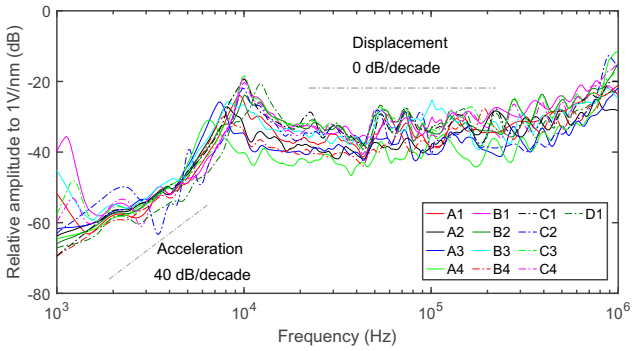

Fig. 10 Summary of displacement-based instrumental responses (colored) over 13 PZT sensors. A1 to D1 represent the label given to the PZT sensors. We have shown displacement- and acceleration-dependence (gray dash dot line) of I_3^d over 10 kHz to 1 MHz and 1 to 6 kHz, respectively.

find that the I_3^a segments overlap well with little vertical shift and the linked I_3^a (blue thick line in the upper part of Fig. 8(b)) is relatively flat from 1.2 to 6 kHz. The PZT sensor is sensitive to time-varying acceleration over this frequency range, where the sensor shows similar responses as accelerometers.

4.3 PZT sensor array: broadband I_3 group

We now extend the analysis of the instrumental response of a single PZT sensor to that of an array of PZT sensors of the same KRN Services model. The detailed arrangement of the PZT sensor array is given in Section 2.2. The single sensor performance over different take-off angles is discussed in Appendix D.

In Fig. 9(a), we show the voltage signals near the first P-wave arrival (blue square) for all sensors, with the take-off angle ranging from 0° to 62.9° caused by a 0.5 mm diameter ball impact. At time $t = 0$, the first P-wave arrives in the ray path θ=0°. We see that the time of the first P-wave arrival has a positive dependence (gray line) on the take-off angle while the first peak amplitude of the P-wave decreases significantly as the take-off angle increases. Also see the similar positive dependence in the first S-wave arrival. Since there are several sensors at the same take-off angle (i.e., θ=42.6° - A3, B2, C3, C4), we find that the corresponding shape of the voltages matches well with each other. But, due to the I_3 variation at the level of uncertainty among these sensors, there exist scaling factors of the absolute amplitude of voltages. Through these observations, we suggest that the proposed experimental configuration realistically captures the elastic wave propagation phenomena using an array of PZT sensors.

We obtain a group of NGFs from all source-receiver pairs and derive the corresponding displacements. The same procedures used for characterization of a single PZT sensor are followed. By using the algorithms described in

Eq. (16), we obtain the valid frequency bandwidth over a broad range of ball diameters for all PZT sensors. In Fig. 9(b), we show the ω_χ^{max} of the valid frequency bandwidth versus the take-off angle θ under ball impacts with different diameters. We find that when θ ranges from 0° to 54.0°, the ω_χ^{max} of all PZT sensors from the same ball impact has minor variations. Moreover, ω_χ^{max} has a positive dependence on the ball size. However, when θ increases to 62.9°, there is weak resultant displacement in the *3*-direction measured by PZT sensor C2. The derived ω_χ^{max} group corresponding to small ball diameters ($<$ 2 mm) are out of order, suggesting that in the characterization experiments, we should keep the epicenter of PZT sensors close to the location of the ball impact. Note that we used conical shaped PZTs throughout these experiments; the corresponding analysis could be quite different for cylindrically shaped PZTs [39].

All the PZT sensors used in this study have been used in laboratory fracturing experiments for some time (more than 3 years). Therefore they are assumed to have a similar response to mechanical vibration but are not exactly identical due to damage of the crystal material as well as uncertain variations in the manufacturing. In Fig. 10, we show well-stacked I_3^d of all the PZT sensors from 1 kHz to 1 MHz . We see that all these PZT sensors have similar displacement- and acceleration-dependence from 10 kHz to 1 MHz and from 1 to 6 kHz, respectively. Remind that for individual calibration of single sensor, the calculated I_3 integrates the effect of the interaction (e.g. static pressure, elastic wave reflection and transmission) between this PZT sensor

and measured object. Regarding the collective calibration of a sensor array, I_3 of single sensor at low frequencies might be affected by interactions between other sensors and measured object. This is not evaluated in the current work but will be considered in future.

5 Conclusions

In this study, we presented a comprehensive FEM analysis of laboratory elastic stress wave modelling to obtain accurate NGFs between an active source and an array of PZT sensors where the modelling parameters are similar to the experimental configuration. To avoid expensive computational costs on separate simulations to calculate the EGFs of a group of ball impacts, we used a unit step force-time function to describe the loading applied at the same location for the ball impacts. The resulting theoretical displacement was readily calculated by performing the convolution between the NGFs and the force-time function of the ball impacts.

To improve computational efficiency, we performed two separate simulations; low-frequency modelling based on a relatively coarse grid (*c-FEM*), and high-frequency modelling based on a relatively fine grid (*f-FEM*). Both models were validated against the reference approach over the high-frequency band such that high-precision FEM solutions are obtained. We performed the low-frequency analysis of wave propagation phenomena which integrated physical-based boundary conditions among the utilized experimental components. We suggest that the results from the *c-FEM* model have better physical founda-

tions. Both the high-frequency validation and low-frequency extension work successfully demonstrate the capabilities of the constructed model to solve the laboratory elastic wave propagation problem.

We performed impacts tests using balls with diameters changing from 0.3 to 3 mm and obtained a group of segmented instrumental responses $I_{3,\chi}^{s,l}$ with various levels of bandwidth overlap. To obtain the broadband I_3, we developed algorithms to accurately pick the bandwidth of $I_{3,\chi}^{s,l}$ by considering the accuracy of FEM solutions and quality of the experimental data. We showed that, to rigorously understand the valid frequency bandwidth of I_3, a broad range of ball diameters are needed. Finally we obtained an accurate I_3 for an array of PZT sensors at different take-off angles.

This study focused on developing methods that can bridge the gap between qualitative analysis and quantitative characterizations of laboratory and *in situ* AEs. Following the proposed methodology, we can absolutely calibrate PZT sensors and thus properly interpret the messages of ground motion from AE monitoring. In future, to study the physics of dynamic failures from near-surface to subsurface conditions, PZT sensors need to be characterized in prior under complicated conditions (i.e. sensors sit inside a pressurised, fluid filled triaxial cell at high-temperature). Our constructed models can potentially be integrated with state-of-the-art multiphysics couplings from COMSOL Multiphysics such that a well-validated FEM model capable at solving (multi-physics) problems of elastic wave propagation can be developed. We can then provide accurate insights into the source properties of microcrack behavior

598 and quantitatively study the damage evolution and fracture propagation in
599 brittle materials over a broadband frequency range and source dimensions.

600 Acknowledgement

601 The authors are indebted to the work and enthusiasm of Mr. Thomas. Mörgeli.
602 He has been instrumental in the study and provided critical input, design
603 strategy and technical expertise for the development the calibration station
604 (Fig. 2(a)). His work is supported through the Rock Physics and Mechanics
605 Laboratory at ETH Zurich. The calibration station was supported by SNF
606 R'equip (Project 170766) Physical constraints on natural and induced earth-
607 quakes using innovative lab-scale experiments: The LabQuake Machine. The
608 authors would also like to thank Elsys company, especially Roman Bertschi for
609 their hardware and software support for this research. Mr. Wu is financially
610 by China Scholarship Council (CSC, No. 201806440037). We kindly thank
611 the review and constructive suggestions from Professor Duncan Agnew and
612 Professor Gregory C. McLaskey.

613 References

614 1. Lockner D (1993) The role of acoustic emission in the study of rock frac-
615 ture. International Journal of Rock Mechanics and Mining Sciences &
616 Geomechanics Abstracts 30(7):883–899
617 2. Grosse CU, Ohtsu M (2008) Acoustic emission testing. Springer Science
618 & Business Media

3. Ishida T, Labuz JF, Manthei G, Meredith PG, Nasseri MHB, Shin K, Yokoyama T, Zang A (2017) ISRM suggested method for laboratory acoustic emission monitoring. Rock Mechanics and Rock Engineering 50(3):665–674
4. Sellers EJ, Kataka MO, Linzer LM (2003) Source parameters of acoustic emission events and scaling with mining-induced seismicity. Journal of Geophysical Research: Solid Earth 108(B9)
5. Li BQ, Einstein HH (2017) Comparison of visual and acoustic emission observations in a four point bending experiment on Barre Granite. Rock Mechanics and Rock Engineering 50(9):2277–2296
6. Li BQ, Einstein HH (2020) Normalized Radiated Seismic Energy From Laboratory Fracture Experiments on Opalinus Clayshale and Barre Granite. Journal of Geophysical Research: Solid Earth 125(3):e2019JB018544
7. Goodfellow SD (2015) Quantitative Analysis of Acoustic Emission from Rock Fracture Experiments. PhD thesis, University of Toronto (Canada)
8. Marty S, Passelègue FX, Aubry J, Bhat HS, Schubnel A, Madariaga R (2019) Origin of High-Frequency Radiation During Laboratory Earthquakes. Geophysical research letters 46(7):3755–3763
9. Selvadurai PA (2019) Laboratory insight into seismic estimates of energy partitioning during dynamic rupture: An observable scaling breakdown. Journal of Geophysical Research: Solid Earth 124:11350–11379
10. Grigoli F, Cesca S, Priolo E, Rinaldi AP, Clinton JF, Stabile TA, Dost B, Fernandez MG, Wiemer S, Dahm T (2017) Current challenges in monitor-

642 ing, discrimination, and management of induced seismicity related to un-
643 derground industrial activities: A European perspective. Reviews of Geo-
644 physics 55(2):310–340
645 11. Kwiatek G, Plenkers K, Dresen G, Group JR (2011) Source parameters
646 of picoseismicity recorded at Mponeng Deep Gold Mine, South Africa:
647 Implications for Scaling Relations. Bulletin of the Seismological Society of
648 America 101(6):2592–2608
649 12. Goodfellow SD, Young RP (2014) A laboratory acoustic emission experi-
650 ment under in situ conditions. Geophysical Research Letters 41(10):3422–
651 3430
652 13. Zang A, Stephansson O, Stenberg L, Plenkers K, Specht S, Milkereit C,
653 Schill E, Kwiatek G, Dresen G, Zimmermann G, Dahm T, Weber M (2016)
654 Hydraulic fracture monitoring in hard rock at 410 m depth with an ad-
655 vanced fluid-injection protocol and extensive sensor array. Geophysical
656 Journal International 208(2):790–813
657 14. Amann F, Gischig V, Evans K, Doetsch J, Jalali R, Valley B, Krietsch H,
658 Dutler N, Villiger L, Brixel B, others (2018) The seismo-hydromechanical
659 behavior during deep geothermal reservoir stimulations: open questions
660 tackled in a decameter-scale in situ stimulation experiment. Solid Earth
661 9(1):115–137
662 15. Manthei G, Plenkers K (2018) Review on in situ acoustic emission mon-
663 itoring in the context of structural health monitoring in mines. Applied
664 Sciences 8(9):1595

665 16. Moradian Z, Einstein HH, Ballivy G (2016) Detection of cracking levels in
666 brittle rocks by parametric analysis of the acoustic emission signals. Rock
667 Mechanics and Rock Engineering 49(3):785–800
668 17. Li BQ, da Silva BG, Einstein H (2019) Laboratory Hydraulic Fracturing of
669 Granite: Acoustic Emission Observations and Interpretation. Engineering
670 Fracture Mechanics
671 18. Hsu NN, Simmons JA, Hardy SC (1978) Approach to acoustic emission
672 signal analysis-theory and experiment
673 19. Breckenridge FR (1982) Acoustic emission transducer calibration by
674 means of the seismic surface pulse. J Acoust Emiss 1:87–94
675 20. Griffin J (2015) Traceability of Acoustic Emission measurements for a
676 proposed calibration method - Classification of characteristics and identi-
677 fication using signal analysis. Mechanical Systems and Signal Processing
678 50-51:757–783
679 21. Johnson LR (1974) Green's function for Lamb's problem. Geophysical
680 Journal International 37(1):99–131
681 22. Lamb H (1904) On the propagation of tremors over the surface of an elastic
682 solid. Philosophical Transactions of the Royal Society of London Series
683 A, Containing papers of a mathematical or physical character 203(359-
684 371):1–42
685 23. Pao Y, Gajewski RR (1977) The generalized ray theory and transient
686 responses of layered elastic solids. Physical Acoustics 13:183–265

687 24. Hsu NN (1985) Dynamic Green's functions of an infinite plate-A computer
688 program. Tech. rep., National Bureau of Standards, Center for Manufac-
689 turing Engineering, Gaithersburg
690 25. McLaskey GC, Glaser SD (2012) Acoustic emission sensor calibration
691 for absolute source measurements. Journal of Nondestructive Evaluation
692 31(2):157–168
693 26. Leser WP, Yuan F, Newman JA (2013) Band-limited Green's Functions for
694 the Quantitative Evaluation of Acoustic Emission using the Finite Element
695 Method. In: 54th AIAA/ASME/ASCE/AHS/ASC Structures, Structural
696 Dynamics, and Materials Conference, p 1655
697 27. Ye R, de Hoop MV, Petrovitch CL, Pyrak-Nolte LJ, Wilcox LC (2016)
698 A discontinuous Galerkin method with a modified penalty flux for the
699 propagation and scattering of acousto-elastic waves. Geophysical Journal
700 International 205(2):1267–1289
701 28. Sause MG, Hamstad MA (2018) Numerical modeling of existing acoustic
702 emission sensor absolute calibration approaches. Sensors and Actuators A:
703 Physical 269:294–307
704 29. Schnabel S, Marklund P, Larsson R (2016) Elastic Waves of a Single
705 Elasto-Hydrodynamically Lubricated Contact. Tribology Letters 65(1):5
706 30. Schnabel S, Golling S, Marklund P, Larsson R (2017) Absolute measure-
707 ment of elastic waves excited by Hertzian contacts in boundary restricted
708 systems. Tribology Letters 65(1):1–11

709 31. Wu BS, McLaskey GC (2018) Broadband calibration of acoustic emis-
710 sion and ultrasonic sensors from generalized ray theory and finite element
711 models. Journal of Nondestructive Evaluation 37(1):8
712 32. Aki K, Richards PG (2002) Quantitative seismology. University Science
713 Books
714 33. Bertschi R (2018) AE-Amp Manual EN. Tech. rep., https://www.elsys-
715 instruments.com/en/products/ae-amp-preamplifier.php
716 34. Reed J (1985) Energy losses due to elastic wave propagation during an
717 elastic impact. Journal of Physics D: Applied Physics 18(12):2329–2337
718 35. Breckenridge F, Proctor T, Hsu N, Fick S, Eitzen D (1990) Transient
719 sources for acoustic emission work. In: Yamaguchi K, Takakashi H, Niit-
720 suma H (eds) Progress in Acoustic Emission, Japanese Society for Non-
721 Destructive Inspection, Tokyo, pp 20–37
722 36. Manthei G (2005) Characterization of acoustic emission sources in a rock
723 salt specimen under triaxial compression. Bulletin of the Seismological
724 Society of America 95(5):1674–1700
725 37. Kwiatek G, Charalampidou EM, Dresen G, Stanchits S (2014) An im-
726 proved method for seismic moment tensor inversion of acoustic emissions
727 through assessment of sensor coupling and sensitivity to incidence angle.
728 Int J Rock Mech Min Sci 65:153–161
729 38. Glaser SD, Weiss GG, Johnson LR (1998) Body waves recorded inside an
730 elastic half-space by an embedded, wideband velocity sensor. The Journal
731 of the Acoustical Society of America 104(3):1404–1412

39. Ono K (2019) Rayleigh wave calibration of acoustic emission sensors and ultrasonic transducers. Sensors (Switzerland) 19(14):3129
40. Bracewell RN (1986) The Fourier transform and its applications, vol 31999. McGraw-Hill New York
41. COMSOL AB (2019) COMSOL Multiphysics® v. 5.5. URL www.comsol.com
42. Cohen M, Jennings PC (1983) Silent Boundary Methods for Transient Analysis. In: Belytschko T, Hughes T (eds) Computational Methods for Transient Analysis, Elsevier
43. Gasch T, Malm R, Ansell A (2016) A coupled hygro-thermo-mechanical model for concrete subjected to variable environmental conditions. International Journal of Solids and Structures 91:143–156
44. Selvadurai APS, Najari M (2013) On the interpretation of hydraulic pulse tests on rock specimens. Advances in Water Resources 53:139–149
45. Selvadurai APS, Najari M (2017) The thermo-hydro-mechanical behavior of the argillaceous Cobourg Limestone. Journal of Geophysical Research: Solid Earth 122(6):4157–4171
46. Jacquey AB, Cacace M (2020) Multiphysics Modeling of a Brittle-Ductile Lithosphere: 1. Explicit Visco-Elasto-Plastic Formulation and Its Numerical Implementation. Journal of Geophysical Research: Solid Earth 125(1):e2019JB018474
47. McLaskey GC, Lockner DA, Kilgore BD, Beeler NM (2015) A robust calibration technique for acoustic emission systems based on momentum

transfer from a ball drop. Bulletin of the Seismological Society of America 105(1):257–271

48. Gu C, Mok U, Marzouk YM, Prieto GA, Sheibani F, Evans JB, Hager BH (2020) Bayesian waveform-based calibration of high-pressure acoustic emission systems with ball drop measurements. Geophysical Journal International 221(1):20–36
49. Askey RA, Roy R (2010) Gamma function. In: NIST Handbook of mathematical functions, chap 5, pp 135–147
50. Hanks TC (1979) b values and $\omega\gamma$ seismic source models: Implications for tectonic stress variations along active crustal fault zones and the estimation of high-frequency strong ground motion. Journal of Geophysical Research: Solid Earth 84(B5):2235–2242
51. Li BQ (2019) Microseismic and Real-time Imaging of Fractures and Microfractures in Barre Granite and Opalinus Clayshale. PhD thesis

A Hertzian impact source

We used the single impact of spherical ball as the mechanical active source to excite stress waves in our transfer plate while the multibounce scenario of ball drop is outside the scope of this study [48]. In Fig. 11(a), when the steel ball instantaneously impacts the steel transfer plate, the force-time function $f_3(t)$ derived from the Hertzian impact theory [34] can be written as

$$\begin{aligned} f_3(t) &= f_{\max} \sin\left(\frac{\pi t}{t_c}\right)^{\frac{3}{2}}, 0 < t \leq t_c, \\ f_3(t) &= 0, t > t_c, \end{aligned} \tag{18}$$

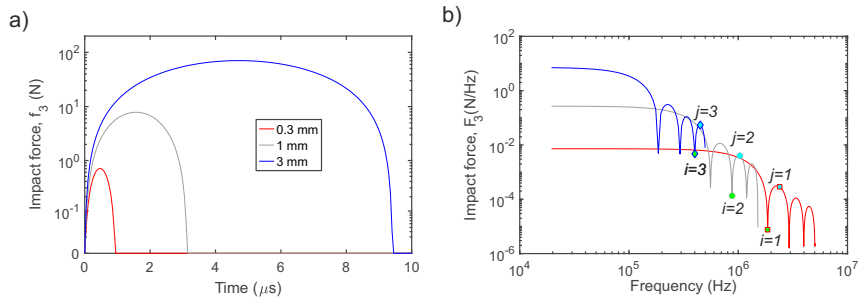

Fig. 11 (a) Force-time function, $f_3(t)$, and (b) its amplitude spectrum, $F_3(\omega)$. For visualization, $f_3(t)$ and $F_3(\omega)$ with diameters of 0.3 mm (red), 1 mm (gray) and 3 mm (blue) are displayed.

where $f_{max} = 1.917\rho_1^{3/5}\left(\delta_1+\delta_2\right)^{-2/5} R_1^2 v_0^{6/5}$ denotes the maximum force of the ball impact, and $t_c = 4.53\left(4\rho_1\pi\left(\delta_1+\delta_2\right)/3\right)^{2/5} R_1 v_0^{-1/5}$ is the contact time between the ball and test specimen. R_1 and ρ_1 are the ball radius and density, respectively. δ_i is a material constant depending on Young's modulus, E_i, and Poisson's ratio, μ_i, of the ball and the plate, that is $\delta_i = (1-\mu_i^2)/(\pi E_i), i = 1, 2$. $v_0 = \sqrt{2gh_d}$ represents the impact velocity due to the free drop motion, where h_d and g are the dropping height and gravitational acceleration, respectively.

The amplitude spectrum of $f_3(t)$, denoted by $F_3(\omega)$, is expressed as

$$F_3(\omega) = 0.2689\frac{\Delta P}{\Gamma\left(\frac{7}{4}+t_c\omega\right)\left|\Gamma\left(\frac{7}{4}-t_c\omega\right)\right|}, \tag{19}$$

where $\Delta P \approx 0.5564(t_c f_{\max})$ is the change in momentum that the ball imparts to the steel transfer plate. Γ is the Gamma function [49].

Due to the properties of $\Gamma(z)$ at non-positive integers, there exists a group of local minima and maxima of $F_3(\omega)$, where

$$\begin{aligned}
&\frac{7}{4} - t_c\omega_0 = 0, -1, -2, ..., -i \Rightarrow \omega_0^i = \frac{i+\frac{7}{4}}{t_c}, \\
&\frac{7}{4} - t_c\omega_p = -\frac{1}{2}, -\frac{3}{2}, ..., -\frac{2j+1}{2} \Rightarrow \omega_p^j = \frac{j+\frac{9}{4}}{t_c}.
\end{aligned} \tag{20}$$

Here i, j are non-negative integers. ω_0^i and ω_p^j are the frequency group corresponding to the local minima $F_3(\omega_0^i)$ of the i th and local maxima $F_3(\omega_p^j)$ of the j th lobe of $F_3(\omega)$. Fig.

11(b) illustrates this. When $F_3(\omega)$ deviates from a flat plateau, spectral energy attenuates rapidly with changes of 2 to 3 orders of magnitude, from 100 kHz to 1 MHz for the force-time function of the 1 mm diameter ball impact (grey lines). The marker symbols positioned by ω_0^i and ω_p^j show the separation of a series of lobes in the spectral energy falloff phase. These characteristics of a series of lobes are useful to validate the theoretical $f_3(t)$ against the calibration at experimental data discussed in Appendix B.1.

B Amplitude spectral analysis in ball impact experiment

To obtain a nearly flat spectrum of the force-time function $f_3(t)$ from 1 kHz to 1 MHz, we dropped a series of steel balls with different diameters from the same height. The impact from balls with a small diameter (i.e., 0.3 mm) has a rise time ($\sim$ 0.5 μs) and imposes a high-frequency mechanical pulse resulting in spectral energy concentrated well below its corner frequency (e.g. $\geq$ 1 MHz). Conversely, the ball impact with relatively large diameter balls (e.g. 3 mm) has a much longer rise time ($\sim$ 4.7 μs) where most of the spectrum energy is concentrated under the low-frequency bandwidth (from 1 to 100 kHz).

Larger diameter (e.g. 10 mm) ball impacts were performed and we found that the response of the PZT sensor used was saturated. For this reason, smaller diameter balls were used. Researchers [30] dropped balls of varying diameter (1.5 to 10 mm) onto a disk plate with a diameter of 103.8 mm. They found that when the contact time is extended by performing larger ball impacts, the elastic waves resulting from the impact and subsequent boundary reflections interacted with each other. As a result, the convolution between $f_3(t)$ and $g_{33}(\mathbf{x}, t)$ does not hold true and $u_3(\mathbf{x}, t)$ cannot be obtained. Therefore, we needed to evaluate the contact time t_c and ensure that the travel time of the elastic waves was (at minimum) twice the plate thickness. Sensor saturation and convolution ineffectiveness are two factors that are under reported in the literature and, considered together, constrained the largest ball diameter to 3 mm in this study.

The same drop height $h_d = 138$ mm was used for all impact tests; this was high enough to generate mechanical vibrations that could be measured by PZT sensors over all take-off

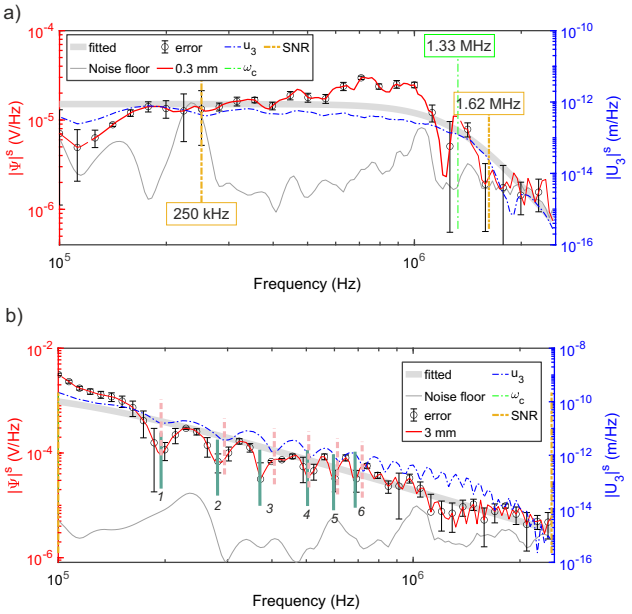

Fig. 12 Amplitude spectra of voltage $|\Psi|^s$ (red line), background noise (thin gray line), fitted model for $|\Psi|^s$ (thick gray line), and displacement $|U_3|^s$ (blue line) of (a) 0.3 mm and (b) 3mm diameter ball impacts over a short duration (80 μs). In (b), a group of local minima of $|U_3|^s$ (pink dash line) and $|\Psi|^s$ (green line) are labelled to show the horizontal offset.

angles. We repeated dropping the steel ball 5 times with 12 diameters (0.3, 0.35, 0.4, 0.5, 0.6, 0.7, 0.8, 1, 1.5, 2, 2.5, 3 mm). We introduced data processing techniques described in Section 2.2 to determine $u_3(\mathbf{x}, t)$ and $\psi(\mathbf{x}, t)$, which were used to obtain the segmented amplitude spectra of displacement $|U_3|$ and voltage $|\Psi|$, from Eqs. 6 and 7, respectively. Note that all the voltage spectra $|\Psi|$ used in this section comes from PZT sensor A1 which located directly beneath the impact point.

B.1 Short-duration excitation (100 kHz to 1 MHz)

In this section, we windowed the raw voltage caused by short-duration (80 μs, denoted by superscript s) excitation of 0.3 and 3 mm ball impacts as shown in the inset region of Fig. 3. The time $t = 0$ is when first P-wave arrives.

826 The amplitude spectra of $|\Psi|^s$ and $|U_3|^s$ due to the 0.3 mm ball impact from 100 kHz to
827 2.5 MHz are shown in Fig. 12(a). Since we are interested in the plateau part of the amplitude
828 spectrum, we need to determine the corresponding corner frequency ω_c. To obtain ω_c, we
829 use the *Omega-n* model [50] to perform fitting of voltage spectra $|\Psi|^s$:

$$\Omega(\omega) = \frac{\Omega_0}{1 + (\omega/\omega_c)^n}. \tag{21}$$

830 In this study, Ω refers to voltage spectra $|\Psi|^s$. The ω_c is determined as 1.33 MHz (green line)
831 in Fig. 12(a) and the fitted result is plotted as the thick gray line. The standard deviation
832 (black error bar) of $|\Psi|^s$ among repeated tests is shown. Minor variations suggest that the
833 ball impact is a repeatable mechanical source and works well at high-frequencies below ω_c.
834 We see the SNR (signal-to-noise ratio) is continuously larger than 1 from almost 250 kHz
835 to 1.62 MHz and this acts as an indicator to crop a valid frequency band of $|\Psi|^s$ in Section
836 4.1.

837 Fig. 12(b) presents the results from a 3 mm ball impact. We note that both $|U_3|^s$ (blue
838 line) and $|\Psi|^s$ (red line) fall off rapidly with an almost constant slope (gray line) fitted from
839 a series of "lobes" while the fitted ω_c is fixed at 100 kHz. This means that we could not crop
840 valid $|U_3|^s$ and $|\Psi|^s$ segmentations from 100 kHz to 1 MHz. We suggest that these lobes
841 are caused by a group of local minima and maxima impact that forces itself in the phase of
842 spectrum energy fall off in accordance with Eq. (20). By labelling the local minima (i.e., *1,*
843 *2, 3, 4, 5, 6, ...*) of $|U_3|^s$ (pink dash line) and $|\Psi|^s$ (green solid line), we find there exists
844 a horizontal offset of frequency. Reed's elastic impact theory does not work accurately at
845 high-frequencies for relatively large diameter ball drops.

846 B.2 Long-duration excitation (1 kHz to 100 kHz)

847 In this section, we extend the short-duration analysis to long-duration case (8000 μs, denoted
848 by superscript l). The raw and windowed $\psi(\mathbf{x}, t)^l$ caused by 0.3 mm and 3 mm ball impacts
849 are shown in Fig. 3.

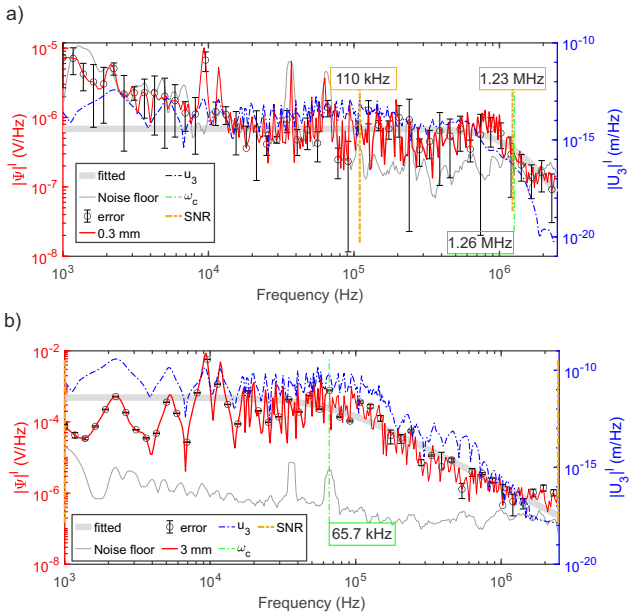

Fig. 13 Amplitude spectra of voltage $|\Psi|^l$ (red line), background noise (thin gray line), fitted model for $|\Psi|^l$(thick gray line), and displacement $|U_3|^l$ (blue line) of (a) 0.3 mm and (b) 3 mm diameter ball impacts over a long duration (8000 μs).

Following the same data processing technique given in Appendix B.1, we obtain the amplitude spectra of voltage $|\Psi|^l$ and displacement $|U_3|^l$ from 0.3 mm ball impact testing. In Fig. 13(a), both $|U_3|^l$ (blue line) and $|\Psi|^l$ (red line) are relatively flat from 1 kHz below the corner frequency ω_c (1.26 MHz, green line) of $|\Psi|^l$. The displacements $|U_3|^l$ are calculated from the *c-FEM* model, which is only validated below 174.6 kHz (see Section 3.3). We see that the amplitude spectrum of the noise floor almost overlaps with or even higher than $|\Psi|^l$ below 110 kHz or beyond 1.23 MHz. Therefore $|\Psi|^l$ valid from 110 to 174.6 kHz can be used with $|U_3|^l$ for further analysis of I_3, see Eq. (8).

By incrementally increasing the ball diameter until 3 mm, we obtain the corresponding $|\Psi|^l$ and $|U_3|^l$ as shown in Fig. 13(b). We find ω_{min} as the minimum between $\omega_c = 65.7$ kHz of $|\Psi|^l$ and 174.6 kHz and determine the valid frequency band from 1 to 65.7 kHz, where the the mean value of SNR is around 20. Both $|U_3|^l$ and $|\Psi|^l$ are relatively flat below ω_c; they have a distinct and similar spectrum shape regarding the local minima and maxima, which indicates the resonance and anti-resonance of the steel transfer plate due to the ball impact.

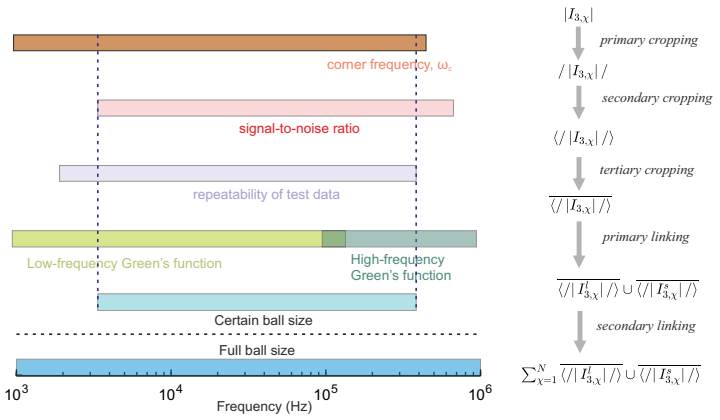

Fig. 14 Schematic drawing of spectral cropping and linking in the proposed algorithm.

By comparing Fig. 13(a) and (b), we find that, with the longer contact times (i.e., from 0.5 to 4.7 μs) associated with larger (i.e., from 0.3 to 3 mm) ball drops, the interaction between elastic waves and the Hertz impact force history could enhance the resonance and anti-resonance observed in the experimental data. The similarity between the experimental data (voltage) and theoretical estimation (displacement) strengthened the reliability of proposed methodology for deriving low-frequency NGFs.

C Spectral cropping and linking

In Fig 14, we present the general principle (left) and flowchart (right) of cropping and linking operations used in Eq. 16. Regarding a ball impact test with certain diameter, top five lines show the transformation from raw $|I_{3,\chi}|$ into well-constrained $\overline{\langle/|\, I^l_{3,\chi}|\,/\rangle} \cup \overline{\langle/|\, I^s_{3,\chi}|\,/\rangle}$. By taking account of a broad range of diameters, we can get the instrumental response from 1 kHz to 1 MHz.

D Effect of take-off angle on broadband I_3 of single PZT sensor

In this section, we aim to evaluate the effect of take-off angle on broadband instrumental response I_3 while maintaining the other factors (e.g. contact, sensor, cable, A/D converter).

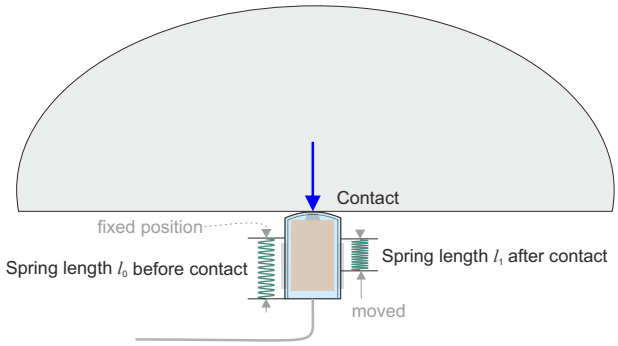

Fig. 15 General schematic of contact manner between the measured object (upper) and PZT sensor.

We perform ball impact tests where the caused ground motion is recorded by the same sensor at 3 take-off angles, $\theta = 0°, 42.6°, 52.4°$, respectively. Ball diameter of 0.4, 1 and 3 mm are selected to cover broadband frequency range (from 1 kHz to 1 MHz) in accordance with the conclusion in Section 4.1. Same cable and A/D converter are utilized through each test. Other experimental parameters refer to Table 1. Fig. 15 shows the contact manner between the measured object (upper) and PZT sensor. By measuring the length of linear springs, we maintain the pressure applied on the PZT sensor tip through tests at different take-off angles. The application of spring-loaded PZT sensors also refers to [51].

We follow the same data processing technique given in Section B.1 to analyze voltage spectra $|\Psi|$ and displacement spectra $|U_3|$ and the proposed algorithm in Section 4.1 to calculate displacement-based instrumental response I_3^d. Fig. 16 shows the I_3^d and associated standard deviations over three take-off angles from 1 kHz to 1 MHz. We notice these I_3^d match well at most frequencies and the standard deviation of I_3^d is mostly below 4 dB. Slight differences in I_3^d could be caused by:

– additional physics not modelled but existing in the realistic elastic wave propagation due to ball impacts. For example, seismic attenuation (e.g. anelastic attenuation, scattering) causing dissipation of energy as elastic waves propagate through the steel plate. Advanced modelling methodology could be expected in future work.

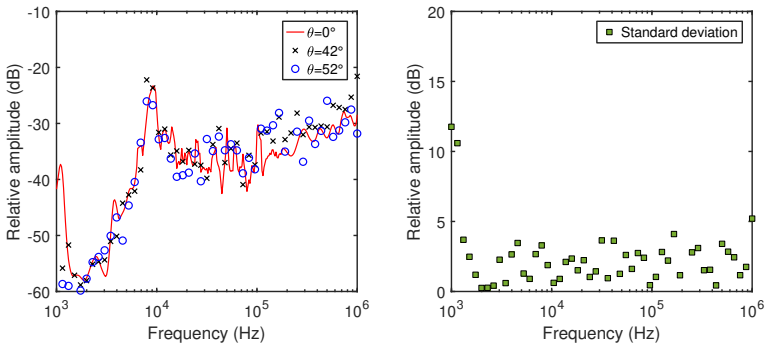

Fig. 16 Displacement-based instrumental responses and standard deviation over take-off angles.

– experimental repeatability. Although we attempt to maintain the potential experimental setting, unexpected variations still occurred through tests.

We take an example to illustrate the effect of slight differences in I_3^d on the source characteristics of impact events. Assume this sensor detects a seismic magnitude of -5.849 (reference) due to 3 mm steel ball impact using the I_3^d from the test of $\theta = 0°$. If using the I_3^d from the test of $\theta = 42.6°, 52.4°$, the inferred seismic magnitudes are -5.855 and -5.833, respectively. Comparing these seismic magnitudes, we conclude that there exist negligible differences in the analyzed source characteristics resulted from different takeoff angles while the same sensor is used through tests.